

Spectroastrometric Study of Ro-vibrational CO Emission from the Herbig Ae star HD 179218 with iSHELL on the NASA Infrared Telescope Facility

SEAN D. BRITTAIN,¹ JOHN S. CARR,² AND JOAN R. NAJITA³

¹*Department of Physics & Astronomy, 118 Kinard Laboratory, Clemson University, Clemson, SC 29634-0978, USA*

²*Naval Research Laboratory, Code 7211, Washington, DC 20375, USA*

³*National Optical Astronomy Observatory, 950 N. Cherry Ave., Tucson, AZ 85719, USA*

ABSTRACT

We present analysis of commissioning M -band data acquired with the infrared echelle spectrograph (iSHELL) on *NASA's Infrared Telescope Facility*. In this paper we describe the delivered performance of the instrument for these M -band observations and the data reduction process. The feasibility of using iSHELL for spectro-astrometry is tested on the Herbig Ae/Be star HD 179218 and we show that sub-milliarcsecond fidelity is achievable.

1. INTRODUCTION

High-resolution spectroscopic observations of CO in disks around young stars have been used to elucidate the evolutionary status of warm gas in disks around young stars (Najita et al. 2000, 2003, 2007; Carr et al. 2001; Carr 2007; Brittain et al. 2003, 2007; Blake & Boogert 2004; Salyk et al. 2009, 2011; Bast et al. 2011; Herczeg et al. 2011; van der Plas et al. 2015; Banzatti & Pontoppidan 2015; Hein Bertelsen et al. 2016). The application of spectro-astrometry (SA) to this observational technique provides additional spatial information about the disk on milli-arcsecond scales (Pontoppidan et al. 2008). It has enabled the identification of non-axisymmetric structures in disks that may point to the presence of disk winds (Pontoppidan et al. 2011) and forming gas giant planets (Brittain et al. 2013).

SA is the measurement of the centroid of the point spread function (PSF) of a spectrum as a function of wavelength or velocity. SA has been

used to study phenomena such as binaries (Bailey 1998; Baines et al. 2004; Porter et al. 2004), outflows (Whelan & Garcia 2008; Davies et al. 2010), and disks (e.g. Acke & van den Ancker 2006; Brittain et al. 2009; Pontoppidan et al. 2011). While the spatial resolution of a PSF is limited to $\sim 1.2D/\lambda$, the relative centroid of the PSF can be measured to a small fraction of that. For a well sampled Gaussian PSF dominated by photon noise, the center of the Gaussian can be measured to an accuracy of $\sim 0.4 \times \text{FWHM}/\text{SNR}$ (Brannigan et al. 2006) where FWHM is the full-width of the PSF at half of its maximum, and SNR is the per pixel signal to noise ratio of the continuum. For $\text{FWHM}=0''.7$ and $\text{SNR} = 100$, we can measure the centroid of each velocity channel of the line to an accuracy of 3 milliarcseconds (1 AU at the distance of HD 179218). By combining multiple lines, this fidelity can be pushed down further.

An important consideration with SA observations is correction for artifacts (Brittain et al. 2015, and references therein). By observing each desired position angle with an anti-parallel

observation, most artifacts can be removed in the data processing. However, grating and slit stability are important to ensure that artifacts are reproducible. Here we present analysis of iSHELL commissioning data to test the feasibility of using this instrument for SA measurements.

iSHELL is a cross-dispersed echelle spectrograph sensitive from 1-5 μ m on the NASA Infrared Telescope Facility (IRTF). The IRTF is a 3m telescope optimized for observations in the infrared. With a 0 $''$.375 slit, the nominal spectral resolution of iSHELL is $\lambda/\Delta\lambda = 75,000$. iSHELL has a 2k H2RG detector that provides coverage of nearly the entire M -band in a single setting (Rayner et al. 2016). Here we present a study of ro-vibrational CO emission from the Herbig Ae/Be star HD 179218.

HD 179218 is a Meeus Group 1 (Meijer et al. 2008) Herbig Ae/Be star with a transition disk (e.g., Menu et al. 2015). The distance to HD 179218 is 293.1 ± 30.5 pc (Gaia Collaboration et al. 2016a,b). This is 20% larger than the distance inferred from Hipparchus data (253 ± 38 pc; van Leeuwen 2007) and 50% larger than the distance inferred from photospheric modeling of the star (201_{-22}^{+25} pc; Montesinos et al. 2009). Where appropriate, we rescale system parameters taken from the literature using the distance reported from Gaia.

Fitting the Balmer lines from the stellar photosphere indicates that $T_{\text{eff}}=9640\pm 250$ K and $\log(g)=3.9\pm 0.2$ (Folsom et al. 2012). The stellar luminosity is $133\pm 28 L_{\odot}$. Using the Siess tracks, this stellar luminosity and effective temperature is consistent with a stellar mass of $3.0\pm 0.1 M_{\odot}$ and stellar radius of $3.3\pm 0.3 R_{\odot}$ (Siess et al. 2000).

Adopting the 1.3mm flux reported by (Alonso-Albi et al. 2009), assuming a disk temperature of 50 K and gas-to-dust mass ratio of 100, the disk mass is $0.07M_{\odot}$. The accretion rate is $1.7\times 10^{-8}M_{\odot} \text{ yr}^{-1}$ (Mendigutía et al. 2017), and

the accreting material is depleted in refractory material indicating that the ratio of gas to dust of the accreting material is ~ 400 Kama et al. (2015). This system is consistent with a transition disk opened by a massive companion.

The inclination of the disk is uncertain. Modeling of the rotational CO line profiles suggest the inclination is $40\pm 10^{\circ}$ (Dent et al. 2005). VLTI/PIONEER data is consistent with a disk inclination of 49° (Lazareff et al. 2017). Fitting the N -band visibilities measured with VLTI/MIDI indicate a disk inclination of $57\pm 2^{\circ}$ and position angle of $23\pm 3^{\circ}$.

In this paper we describe the observations and data reduction (section 2). Next we characterized the reduced spectra and spectroastrometric signal (section 3). We compare the data acquired with iSHELL to CRIRES observations of the same source (section 4), and conclude with an analysis of the excitation of the gas (section 5) and suggest future work.

2. OBSERVATIONS

The data were acquired October 11, 2016 as part of the science commissioning program for iSHELL. The observation log is summarized in Table 1. A total of 30 minutes of data were taken using the M2 grating setting and a slit width of 0 $''$.375. The observations were taken in an ABBA nod pattern in order to cancel the sky background to first order. At each position, the integration time was 15 seconds and 2 coadds. The observations were divided into two sets. For the first 15 minutes of integration, the position angle was fixed at 23° east of north. The slit was then rotated to 203° east of north for the second half of the observations. A telluric standard, HD 177724, was observed at a similar airmass. Flats were taken immediately following the observation before the grating was moved.

The two sets of data from HD179218 and the telluric standard were reduced individually us-

ing interactive software written in IDL. The median of the “A” files and the median of the “B” files were used to flag cosmic ray hits. The non-flagged pixels were then averaged.

The M2 setting includes 16 orders covering 1910.6 - 2217.5 cm^{-1} . The coverage of the orders ranges from $\sim 16 \text{ cm}^{-1}$ at the red end to 18.5 cm^{-1} at the blue end. The gap between orders ranges from 3 cm^{-1} at the red end to 1 cm^{-1} at the blue end. Thus the total coverage of the M-band is $\sim 90\%$.

Custom software was written in IDL for reducing this data following the process described in (Brittain 2004). Our approach differs from the iSHELL tool in that each order is reduced separately and the rectified 2-D spectra are saved for SA measurements. To reduce the data, the user selects several points along the A and B beam, and a polynomial is fit to these points. The mid-point of the PSF is defined for each column of the order and used to create a box to extract the order to be reduced. This region is divided by the normalized flat and the A and B frames are subtracted to produce a flat-fielded sky subtracted image.

A refined trace along the spectra in the order is found by fitting a Moffat function to the PSF in each column using MPFIT (Markwardt 2009). The bad pixel mask provided by the observatory is used to exclude bad pixels from the fit. Columns where the fit diverges by more than 3 pixels from the centroid defined by the user are excluded (this is usually because there is little continuum in a given column). Deviant pixels are flagged and replaced by the value of the fit. A third-degree polynomial is fit to the center of the PSF in each column and the rows are shifted so that the A and B beams are rectified on the array.

The same shift is applied to the non-sky subtracted A and B frames. The top half of the A-frame and bottom half of the B-frame (where there is no stellar spectrum) are combined to

create a sky emission frame. Each row of this frame is fit with radiance model generated by the Sky Synthesis Program (SSP; Kunde & Maguire 1974) which accesses the HITRAN2000 molecular line database (Rothman et al. 2003). The first row is fit interactively, then the wavelength solution is refined by optimizing the fit of the model to each row of the sky spectrum. The rows are then interpolated to the solution of the middle row so that the spectra are rectified in the spectral dimension as well.

The A and B beam are extracted using rectangular extraction of the full width at 10% of the maximum. The A and B beams are averaged and fit with a transmittance function produced by the SSP to refine the wavelength solution. The spectra are then normalized, and the spectra of HD 179218 are divided by the spectra of the telluric standard whose airmass is scaled in order to minimize the residuals of the telluric absorption lines. Regions where the atmospheric transmittance is less than 50% are excluded. The spectra are scaled to flux units by adopting the continuum flux provided by the ALLWISE data release, which is $4.82 \pm 0.49 \text{ Jy}$ (Cutri et al. 2013).

To measure the spectro-astrometric signal of the emission lines, the centroids of the A and B rows of the rectified array are measured for each column and then averaged. The centroid measurements of the parallel and anti-parallel position angles are then subtracted and divided by two. The spectra and spectroastrometric measurements are presented in Figure 1.

3. RESULTS

The SNR of the spectra near the center of the order ranges from 100-120 near 2145 cm^{-1} to 120-140 near 2011 cm^{-1} (Fig 1). The orders at either edge of the band have a considerably lower SNR (~ 35 near 1915 cm^{-1} and 2210 cm^{-1}). Moving from the center of the order to the edges, the SNR decreases modestly as well. The average SNR of the entire spectrum is 55

and is limited by systematic features from mis-canceled sky lines.

The FWHM of the PSF ranges from 3.60 pixels in order 102 ($\tilde{\nu}_0 \sim 1976 \text{ cm}^{-1}$) to 3.46 pixel in order 113 ($\tilde{\nu}_0 \sim 2189 \text{ cm}^{-1}$). For the plate scale of IRTF in the M -band (160 mas/pixel) this corresponds to a FWHM=560 mas. There is a weak trend across the orders indicating an improvement in the imaging quality of 1.4 mas per order. The 22 mas improvement is comparable to the change in the diffraction limit (420 mas near 1976 cm^{-1} to 380 mas near 2189 cm^{-1}).

There is a significant fringe running through the data at the 5% level (Fig. 2). This is mostly removed by dividing by the telluric standard. There is some residual structure left in each spectrum; however, the SNR is dominated in most regions by the quality of the telluric correction.

The iSHELL exposure time calculator (ETC) predicts a SNR of 120/column for an $M=3.95$ magnitude star observed with a $0.375''$ slit for 30 min with a $0.56''$ PSF. Thus the ETC and delivered signal to noise are broadly consistent for regions where there is continuum near the peak of the blaze.

As noted in section 2, the fidelity of the centroid measurement is $0.4 \times \text{FWHM}/\text{SNR}$ (Branigan et al. 2006). The FWHM of the PSF is 560 mas, so the fidelity of the centroid measurement at the blue end of the array should range from 1.9-2.2 mas near 2145 cm^{-1} and 1.6-1.9 mas near 2011 cm^{-1} . The measured standard deviations of the centroid measurements near 2145 cm^{-1} and 2011 cm^{-1} are 2.2 mas and 2.1 mas respectively. The standard deviations of the centroid measurements are slightly higher than predicted, pointing to systematic effects.

The origin of this discrepancy is unclear. In principle it could be caused by inconsistencies in the rectification of the array observed at the parallel slit position and the rectification of the array observed at the anti-parallel slit position.

However, comparison of the rectification of the arrays does not show any differences. Another possibility is that there are subtle differences in the flat fielding due to different amounts of flexure in the system between the observation of the star and the target. Finally, there is some fringing in the system. If the shift in the center of the PSF due to the fringes is not repeated exactly, this could also result in some remnant structure. To the extent that these effects increase the noise of our spectro-astrometric measurement, the effect is to increase the standard deviation of our measurement by less than 10%. The standard deviation of the centroid measurement from 1950 cm^{-1} - 2200 cm^{-1} is 4.3mas which is consistent with expectations for the average SNR over the full array (55).

The broad wavelength coverage provides simultaneous observation of many CO lines. We measured the equivalent width of 155 ro-vibrational CO lines spanning $v'=1$ through $v'=3$ for ^{12}CO and $v'=1$ for ^{13}CO (Table 2). Stacking these lines provides enhanced sensitivity of our measurement of the line profile and the spectro-astrometric signal (Figs. 3-7). The $v=1-0$ line profile is the average of 48 transitions resulting in a SNR along the continuum of 520 and the standard deviation of the centroid measurement is 0.44mas (Fig. 3). For a system limited by photon noise, the SNR would improve to 830 and the centroid measurement to 0.28mas. Our results do not show this level of improvement because no attempt was made to mask the signal from emission not included in the average.

4. COMPARISON TO CRIRES

HD 179218 was observed June 16, 2007 with *CRİRES* on the *European Southern Observatory Very Large Telescope (VLT)* (van der Plas et al. 2015). *CRİRES* is a high resolution ($R \sim 100,000$) near infrared spectrograph that observes a single order at a time. The spectrum covered three regions centered near 2150 cm^{-1} ,

2105 cm^{-1} , and 1990 cm^{-1} , and the integration times were 20 min, 10 min, and 16 min respectively. The spectral grasp of each setting spans $\sim 50 \text{ cm}^{-1}$ in the M -band. The instrument uses four detectors, and there is a $\sim 3 \text{ cm}^{-1}$ gap between each detector. Two overlapping regions of the spectrum of HD 179218 acquired with CRIRES and iSHELL are presented in Figure 8. These regions were selected due to the minimal telluric lines. The SNR of the continuum from 2009.6 cm^{-1} - 2010.6 cm^{-1} is 124 for the CRIRES spectrum which is similar to the iSHELL spectrum (122 in 30 minutes; Fig. 8). Similarly the SNR of the continuum from 2144.4 cm^{-1} to 2145.1 cm^{-1} is 127 for the CRIRES spectrum and 131 for the iSHELL spectrum.

The large spectral grasp of iSHELL provides a significant advantage when stacking multiple transitions. The average profile of the $v=1-0$ CO lines highlights the increase in sensitivity (Fig. 9). The lines averaged together to create this profile resulted from a total of 46 minutes of integration time with CRIRES on the VLT. The average profile of the $v=1-0$ CO lines constructed from the iSHELL spectra required 30 minutes of integration. The improvement in the quality of the line profile is striking. From the improved line profile, we can place a much tighter constraint on the radial distribution of the CO emission. One must exercise caution in interpreting the average line profile because the dense forest of CO lines results in significant blending from $v=2-1$, $v=3-2$ and $^{13}\text{CO } v=1-0$ lines. The impact of line blending can be assessed by modeling the spectrum and comparing the average profile of the observed line and synthetic line. Such modeling is beyond the scope of this paper. However to quantify the FWHM of the lines, we fit a flat-topped Gaussian function to each line profile given by

$$g = a(0)(1 - \exp(-a(1)e^{-u^2})) + a(4) \quad (1)$$

where $u = ((v - a(2))/a(3))^3$ and the FWHM is given by

$$2 \times a(3) \times \sqrt{-\ln(\ln(2)/a(1))}. \quad (2)$$

This is the functional form for an optically thick emission line, though here we use it to capture the flat-topped shape of the emission lines. For each fit, we fixed the line center at 0 km s^{-1} . From the fits we find that the FWHM is higher for the hotband transitions than for the $v=1-0$ transitions (Figs. 3-7). The fit parameters and FWHM of each average profile are presented in Table 3.

5. EXCITATION ANALYSIS

We can estimate the column density and opacity of the CO lines arising in the disk around HD 179218. For optically thin lines, the number of molecules in state i is given by $N_i = L_{ij}/hc\tilde{\nu}A_{ij}$. Assuming the rotational levels of the CO are in local thermodynamic equilibrium, the number of emitting molecules in state i is related to the total number of molecules in a given vibrational band by

$$N_i = g_i N e^{-E_i/kT}/Q \quad (3)$$

where g_i is the statistical weight of the upper state, E_i is the energy of the upper level, T is the rotational temperature, and Q is the partition function. By plotting $\ln(N_i/g_i)$ vs E_i/k , one can determine the rotational temperature from the negative reciprocal of the slope and the total number of emitters from the y-intercept (Fig. 10). The rotational temperatures of the $^{12}\text{CO } v=1-0$, $v=2-1$, $v=3-2$, and $^{13}\text{CO } v=1-0$ lines are $640 \pm 10 \text{ K}$, $770 \pm 30 \text{ K}$, $1270 \pm 120 \text{ K}$, and 630 ± 90 respectively. The FWHM of the average profile of the $v=1-0$ ^{12}CO and ^{13}CO lines is about 3 km s^{-1} narrower than the FWHM of the average profile of the $v=2-1$ and $v=3-2$ ^{12}CO lines (Table 3). This is consistent with the higher vibrational bands originating closer to the star.

Unlike, van der Plas (2015), we do not detect any emission lines from $v'=4$ (Fig. 6). The population of the vibrational states indicates a vibrational temperature of 1850 ± 90 K. While the flux of the $v=1-0$ emission lines is comparable in our data and the data presented by van der Plas et al. (2015), the $v=4-3$ lines are at least 4-8 times fainter. This suggests that there is significant temperature variability in this system. The fact that the vibrational temperature is greater than the rotational temperature of the gas is consistent with UV fluorescence (e.g., Brittain et al. 2007), however, it is also possible that the gas is marginally optically thick and we are underestimating the rotational temperature.

The excitation diagrams are not linear and are indicative of a large temperature range in the emitting region of the disk and/or optically thick ro-vibrational lines (Fig. 10). The line center opacity of a line is given by

$$\tau_i = \Sigma_i A_{ij} (1 - e^{-hc\tilde{\nu}/kT}) / 8\pi^3/2 \tilde{\nu}^3 b \quad (4)$$

where Σ_i is the column density of CO molecules in state i , A_{ij} is the Einstein A coefficient for the transition, $\tilde{\nu}$ is the wavenumber of the transition, and b is the intrinsic width of the line. We can get a rough idea of the line center opacity of the $v=1-0$ lines by estimating the emitting area of the disk from the CO line profile. The half-width at zero intensity (HWZI) provides a measure of the inner extent of the CO emission and half of the peak separation (HPS) of the line provides a measure of the outer extent of the CO emission. The HWZI is ~ 20 km s^{-1} and the HPS is ~ 6 km s^{-1} . For an inclination of 40° , this translates to an emitting area of $\sim 10^{30}$ cm^2 . At a temperature of 640 K, the most populated state we measure ($v'=1$, $J'=15$) is 3×10^{40} molecules. Thus the surface density of molecules in that state is 3×10^{10} molecules cm^{-2} . The line center opacity of that transition is $\sim 10^{-5}$ for $b=1$ km s^{-1} . Thus the lines are extremely optically thin. This is expected for

lines populated by UV fluorescence (Brittain et al. 2009). A more quantitative measure of the CO distribution and abundance requires spectral synthesis of the spectrum and fitting to the SA signal (e.g., Brittain et al. 2007), which is the subject of future work.

6. CONCLUSIONS

We have measured the fundamental ro-vibrational CO spectrum from the transition disk of HD 179218 using iSHELL on the IRTF. The lines are resolved, symmetric, and consistent with the line profile observed with CRIRES in 2007. We have also measured the spectro-astrometric signal of the CO lines and the signal is qualitatively consistent with gas emission in Keplerian orbit. In a future paper we will compare this source to other measurements of CO emission in transition disks and model the spectro-astrometric measurement and emission lines spectrum.

This work highlights the utility of iSHELL for M -band spectroscopy of young stars and for spectroastrometry. Sub-milliarcsecond fidelity is achievable with this instrument on the IRTF. The ETC provides a reliable estimate of the instrument sensitivity, though there is significant variation across the orders. The comparison of iSHELL and CRIRES highlights the high science value of modest aperture 3m class telescopes when equipped with 21st century instrumentation. When the scientific objective depends on the observation of multiple lines spanning the photometric band, the much larger spectral grasp of iSHELL enhances its efficiency. While an updated CRIRES with a cross-dispersed spectrograph promises similar gains in efficiency, iSHELL will remain a valuable counterpart in the northern hemisphere.

SDB, JSC, and JRN were visiting Astronomers at the Infrared Telescope Facility, which is operated by the University of Hawaii under contract NNH14CK55B with the National Aeronautics

and Space Administration. Work by SDB was performed in part at the National Optical Astronomy Observatory. NOAO is operated by the Association of Universities for Research in Astronomy (AURA), Inc. under a cooperative agreement with the National Science Foundation. SDB also acknowledges support from this work by NASA Agreement No. NXX15AD94G; NASA Agreement No. NNX16AJ81G; and NSF-AST 1517014. JRN acknowledges the stimulating research environment supported by NASA Agreement No. NNX15AD94G to the "Earths in Other Solar Systems" program.

Basic research in infrared astronomy at the Naval Research Laboratory is supported by 6.1 base funding. This work has made use of data from the European Space Agency mission *Gaia* (<https://www.cosmos.esa.int/gaia>), processed by the *Gaia* Data Processing and Analysis Consortium (DPAC, <https://www.cosmos.esa.int/web/gaia/dpac/consortium>). Funding for the DPAC has been provided by national institutions, in particular the institutions participating in the *Gaia* Multilateral Agreement.

Facilities:

Facility: Infrared Telescope Facility (iSHELL)

REFERENCES

- Acke, B., & van den Ancker, M. E. 2006, *A&A*, 449, 267
- Ádámkóvics, M., Najita, J. R., & Glassgold, A. E. 2016, *ApJ*, 817, 82
- Alonso-Albi, T., Fuente, A., Bachiller, R., et al. 2009, *A&A*, 497, 117
- Bailey, J. A. 1998, in *Proc. SPIE*, Vol. 3355, Optical Astronomical Instrumentation, ed. S. D'Odorico, 932–939
- Baines, D., Oudmaijer, R. D., Mora, A., et al. 2004, *MNRAS*, 353, 697
- Banzatti, A., & Pontoppidan, K. M. 2015, *ApJ*, 809, 167
- Bast, J. E., Brown, J. M., Herczeg, G. J., van Dishoeck, E. F., & Pontoppidan, K. M. 2011, *A&A*, 527, A119
- Blake, G. A., & Boogert, A. C. A. 2004, *ApJL*, 606, L73
- Brannigan, E., Takami, M., Chrysostomou, A., & Bailey, J. 2006, *MNRAS*, 367, 315
- Brittain, S. D. 2004, PhD thesis, UNIVERSITY OF NOTRE DAME
- Brittain, S. D., Carr, J. S., Najita, J. R., Quanz, S. P., & Meyer, M. R. 2014, *ApJ*, 791, 136
- Brittain, S. D., Najita, J. R., & Carr, J. S. 2009, *ApJ*, 702, 85
- . 2015, *Ap&SS*, 357, 54
- Brittain, S. D., Najita, J. R., Carr, J. S., et al. 2013, *ApJ*, 767, 159
- Brittain, S. D., Rettig, T. W., Simon, T., et al. 2003, *ApJ*, 588, 535
- Brittain, S. D., Simon, T., Najita, J. R., & Rettig, T. W. 2007, *ApJ*, 659, 685
- Brown, J. M., Blake, G. A., Dullemond, C. P., et al. 2007, *ApJL*, 664, L107
- Carr, J. S. 2007, in *IAU Symposium*, Vol. 243, Star-Disk Interaction in Young Stars, ed. J. Bouvier & I. Appenzeller, 135–146
- Carr, J. S., Mathieu, R. D., & Najita, J. R. 2001, *ApJ*, 551, 454
- Cutri, R. M., Wright, E. L., Conrow, T., et al. 2013, Explanatory Supplement to the AllWISE Data Release Products, Tech. rep.
- Davies, B., Lumsden, S. L., Hoare, M. G., Oudmaijer, R. D., & de Wit, W.-J. 2010, *MNRAS*, 402, 1504
- Dent, W. R. F., Greaves, J. S., & Coulson, I. M. 2005, *MNRAS*, 359, 663
- Fedele, D., Pascucci, I., Brittain, S., et al. 2011, *ApJ*, 732, 106
- Folsom, C. P., Bagnulo, S., Wade, G. A., et al. 2012, *MNRAS*, 422, 2072
- Gaia Collaboration, Brown, A. G. A., Vallenari, A., et al. 2016a, *A&A*, 595, A2
- Gaia Collaboration, Prusti, T., de Bruijne, J. H. J., et al. 2016b, *A&A*, 595, A1
- Goto, M., Usuda, T., Dullemond, C. P., et al. 2006, *ApJ*, 652, 758
- Hein Bertelsen, R. P., Kamp, I., van der Plas, G., et al. 2016, *A&A*, 590, A98
- Herbig, G. H. 1960, *The Astrophysical Journal Supplement*, 4, 337

- Herbig, G. H., & Bell, K. R. 1988, Third Catalog of Emission-Line Stars of the Orion Population : 3 : 1988
- Herczeg, G. J., Brown, J. M., van Dishoeck, E. F., & Pontoppidan, K. M. 2011, *A&A*, 533, A112
- Kama, M., Folsom, C. P., & Pinilla, P. 2015, *A&A*, 582, L10
- Kunde, V. R., & Maguire, W. C. 1974, *JQSRT*, 14, 803
- Lazareff, B., Berger, J.-P., Kluska, J., et al. 2017, *A&A*, 599, A85
- Maaskant, K. M., Honda, M., Waters, L. B. F. M., et al. 2013, *A&A*, 555, A64
- Markwardt, C. B. 2009, in *Astronomical Society of the Pacific Conference Series*, Vol. 411, *Astronomical Data Analysis Software and Systems XVIII*, ed. D. A. Bohlender, D. Durand, & P. Dowler, 251
- Meeus, G., Waters, L. B. F. M., Bouwman, J., et al. 2001, *A&A*, 365, 476
- Meijer, J., Dominik, C., de Koter, A., et al. 2008, *A&A*, 492, 451
- Mendigutía, I., Oudmaijer, R. D., Mourard, D., & Muzerolle, J. 2017, *MNRAS*, 464, 1984
- Menu, J., van Boekel, R., Henning, T., et al. 2015, *A&A*, 581, A107
- Montesinos, B., Eiroa, C., Mora, A., & Merín, B. 2009, *A&A*, 495, 901
- Najita, J., Carr, J. S., & Mathieu, R. D. 2003, *ApJ*, 589, 931
- Najita, J. R., Carr, J. S., Glassgold, A. E., & Valenti, J. A. 2007, *Protostars and Planets V*, 507
- Najita, J. R., Edwards, S., Basri, G., & Carr, J. 2000, *Protostars and Planets IV*, 457
- Pontoppidan, K. M., Blake, G. A., & Smette, A. 2011, *ApJ*, 733, 84
- Pontoppidan, K. M., Blake, G. A., van Dishoeck, E. F., et al. 2008, *ApJ*, 684, 1323
- Porter, J. M., Oudmaijer, R. D., & Baines, D. 2004, *A&A*, 428, 327
- Rayner, J., Tokunaga, A., Jaffe, D., et al. 2016, in *Proc. SPIE*, Vol. 9908, *Ground-based and Airborne Instrumentation for Astronomy VI*, 990884
- Rothman, L. S., Barbe, A., Benner, D. C., et al. 2003, *JQSRT*, 82, 5
- Salyk, C., Blake, G. A., Boogert, A. C. A., & Brown, J. M. 2009, *ApJ*, 699, 330
- . 2011, *ApJ*, 743, 112
- Siess, L., Dufour, E., & Forestini, M. 2000, *A&A*, 358, 593
- Thi, W. F., Kamp, I., Woitke, P., et al. 2013, *A&A*, 551, A49
- Valenti, J. A., Fallon, A. A., & Johns-Krull, C. M. 2003, *ApJS*, 147, 305
- van der Plas, G., van den Ancker, M. E., Waters, L. B. F. M., & Dominik, C. 2015, *A&A*, 574, A75
- van Leeuwen, F. 2007, *A&A*, 474, 653
- Whelan, E., & Garcia, P. 2008, in *Lecture Notes in Physics*, Berlin Springer Verlag, Vol. 742, *Jets from Young Stars II*, ed. F. Bacciotti, L. Testi, & E. Whelan, 123

Table 1. Journal of Observations

Star	M_m	Int Time	PA
		(m)	
HD 177724	2.97	15	75.5°
HD 179218	3.87	15	23°
HD 179218	3.87	15	203°

Table 2. Observed CO lines

v'	v''	ID	$\tilde{\nu}$	A	E'	EqW
			cm ⁻¹	s ⁻¹	cm ⁻¹	cm ⁻¹
¹² C ¹⁶ O lines						
1	0	R(14)	2196.66	18.3	3681.71	0.0141 ± 0.0010
1	0	R(13)	2193.36	18.1	3624.64	0.0154 ± 0.0011
1	0	R(12)	2190.02	18.0	3571.37	0.0131 ± 0.0004
1	0	R(11)	2186.64	17.9	3521.89	0.0164 ± 0.0013
1	0	R(10)	2183.22	17.7	3476.21	0.0120 ± 0.0004
1	0	R(8)	2176.28	17.4	3396.26	0.0138 ± 0.0007
1	0	R(7)	2172.76	17.2	3361.99	0.0143 ± 0.0007
1	0	R(6)	2169.20	16.9	3331.52	0.0126 ± 0.0006
1	0	R(5)	2165.60	16.6	3304.86	0.0147 ± 0.0004
1	0	R(4)	2161.97	16.3	3282.00	0.0147 ± 0.0073
1	0	R(3)	2158.30	15.9	3262.96	0.0146 ± 0.0004
1	0	R(2)	2154.60	15.2	3247.72	0.0100 ± 0.0003
1	0	R(1)	2150.86	14.1	3236.29	0.0133 ± 0.0004
1	0	R(0)	2147.08	11.7	3228.67	0.0088 ± 0.0005
1	0	P(1)	2139.43	34.7	3224.86	0.0090 ± 0.0010
1	0	P(2)	2135.55	23.0	3228.67	0.0070 ± 0.0020
1	0	P(3)	2131.63	20.6	3236.29	0.0130 ± 0.0013
1	0	P(4)	2127.68	19.5	3247.71	0.0176 ± 0.0005
1	0	P(5)	2123.70	18.9	3262.96	0.0135 ± 0.0004
1	0	P(6)	2119.68	18.4	3282.00	0.0135 ± 0.0007
1	0	P(7)	2115.63	18.1	3304.86	0.0144 ± 0.0014
1	0	P(8)	2111.54	17.8	3331.52	0.0117 ± 0.0004
1	0	P(9)	2107.42	17.6	3361.98	0.0150 ± 0.0030
1	0	P(10)	2103.27	17.3	3396.26	0.0171 ± 0.0034
1	0	P(11)	2099.08	17.2	3434.33	0.0145 ± 0.0004
1	0	P(12)	2094.86	17.0	3476.21	0.0114 ± 0.0011
1	0	P(13)	2090.61	16.8	3521.89	0.0136 ± 0.0027
1	0	P(14)	2086.32	16.7	3571.37	0.0108 ± 0.0011
1	0	P(15)	2082.00	16.5	3624.64	0.0146 ± 0.0029
1	0	P(17)	2073.26	16.3	3742.57	0.0114 ± 0.0006

Table 2 continued

Table 2 (*continued*)

v'	v''	ID	$\tilde{\nu}$	A	E'	EqW
			cm^{-1}	s^{-1}	cm^{-1}	cm^{-1}
1	0	P(18)	2068.85	16.1	3807.22	0.0174 ± 0.0035
1	0	P(20)	2059.91	15.9	3947.88	0.0158 ± 0.0047
1	0	P(25)	2037.03	15.3	4365.67	0.0084 ± 0.0008
1	0	P(26)	2032.35	15.2	4460.54	0.0043 ± 0.0001
1	0	P(27)	2027.65	15.1	4559.17	0.0056 ± 0.0006
1	0	P(28)	2022.91	14.9	4661.56	0.0056 ± 0.0011
1	0	P(29)	2018.15	14.8	4767.71	0.0081 ± 0.0008
1	0	P(30)	2013.35	14.7	4877.60	0.0039 ± 0.0012
1	0	P(31)	2008.53	14.6	4991.25	0.0058 ± 0.0017
1	0	P(32)	2003.67	14.5	5108.63	0.0011 ± 0.0010
2	1	R(22)	2194.46	36.8	6381.69	0.0061 ± 0.0012
2	1	R(21)	2191.50	36.6	6295.17	0.0053 ± 0.0011
2	1	R(19)	2185.45	36.2	6133.33	0.0069 ± 0.0014
2	1	R(18)	2182.36	36.0	6058.02	0.0013 ± 0.0013
2	1	R(14)	2169.66	35.1	5794.30	0.0048 ± 0.0010
2	1	R(13)	2166.39	34.8	5737.76	0.0061 ± 0.0006
2	1	R(12)	2163.08	34.6	5684.97	0.0050 ± 0.0015
2	1	R(10)	2156.36	34.0	5590.70	0.0053 ± 0.0005
2	1	R(8)	2149.49	33.3	5511.48	0.0040 ± 0.0013
2	1	R(7)	2146.00	32.9	5477.52	0.0067 ± 0.0013
2	1	R(6)	2142.47	32.5	5447.33	0.0013 ± 0.0013
2	1	R(5)	2138.91	32.0	5420.91	0.0037 ± 0.0010
2	1	R(4)	2135.31	31.3	5398.26	0.0032 ± 0.0003
2	1	R(0)	2120.57	22.5	5345.43	0.0020 ± 0.0010
2	1	P(1)	2112.98	66.7	5341.65	0.0024 ± 0.0013
2	1	P(2)	2109.14	44.2	5345.43	0.0031 ± 0.0006
2	1	P(3)	2105.26	39.6	5352.98	0.0028 ± 0.0006
2	1	P(4)	2101.34	37.5	5364.29	0.0012 ± 0.0013
2	1	P(5)	2097.39	36.2	5379.39	0.0030 ± 0.0009
2	1	P(6)	2093.41	35.4	5398.27	0.0022 ± 0.0010
2	1	P(7)	2089.39	34.7	5420.91	0.0091 ± 0.0005
2	1	P(8)	2085.34	34.2	5447.33	0.0024 ± 0.0010
2	1	P(11)	2072.99	33.0	5549.20	0.0035 ± 0.0001
2	1	P(14)	2060.33	32.0	5684.97	0.0046 ± 0.0014
2	1	P(15)	2056.05	31.8	5737.76	0.0059 ± 0.0002
2	1	P(16)	2051.73	31.5	5794.30	0.0039 ± 0.0010
2	1	P(17)	2047.38	31.2	5854.60	0.0037 ± 0.0001
2	1	P(18)	2043.00	31.0	5918.66	0.0022 ± 0.0007
2	1	P(19)	2038.58	30.7	5986.46	0.0045 ± 0.0005
2	1	P(20)	2034.14	30.5	6058.03	0.0050 ± 0.0005
2	1	P(21)	2029.66	30.3	6133.33	0.0031 ± 0.0005
2	1	P(23)	2020.60	29.8	6295.17	0.0010 ± 0.0010
2	1	P(24)	2016.03	29.6	6381.70	0.0022 ± 0.0006
2	1	P(25)	2011.42	29.4	6471.96	0.0023 ± 0.0006
2	1	P(27)	2002.12	28.9	6663.68	0.0010 ± 0.0010
3	2	R(30)	2189.31	55.0	9281.07	0.0027 ± 0.0008

Table 2 continued

Table 2 (*continued*)

v'	v''	ID	$\tilde{\nu}$	A	E'	EqW
			cm^{-1}	s^{-1}	cm^{-1}	cm^{-1}
3	2	R(27)	2181.33	54.3	8946.45	0.0020 ± 0.0010
3	2	R(26)	2178.59	54.0	8842.27	0.0051 ± 0.0010
3	2	R(25)	2175.81	53.7	8741.76	0.0010 ± 0.0010
3	2	R(23)	2170.14	53.2	8551.84	0.0032 ± 0.0005
3	2	R(22)	2167.25	52.9	8462.42	0.0020 ± 0.0005
3	2	R(21)	2164.31	52.6	8376.69	0.0030 ± 0.0005
3	2	R(20)	2161.34	52.3	8294.67	0.0024 ± 0.0005
3	2	R(18)	2155.28	51.8	8141.75	0.0029 ± 0.0005
3	2	R(17)	2152.20	51.4	8070.86	0.0015 ± 0.0005
3	2	R(16)	2149.08	51.1	8003.68	0.0017 ± 0.0005
3	2	R(14)	2142.72	50.5	7880.48	0.0010 ± 0.0005
3	2	R(12)	2136.21	49.7	7772.16	0.0006 ± 0.0005
3	2	R(11)	2132.91	49.3	7723.6	0.0014 ± 0.0005
3	2	R(10)	2129.56	48.9	7678.76	0.0028 ± 0.0005
3	2	R(9)	2126.18	48.5	7637.66	0.0026 ± 0.0010
3	2	R(8)	2122.76	48.0	7600.28	0.0020 ± 0.0010
3	2	R(7)	2119.30	47.4	7566.63	0.0018 ± 0.0010
3	2	R(5)	2112.29	46.0	7510.56	0.0018 ± 0.0010
3	2	R(4)	2108.72	45.1	7488.12	0.0034 ± 0.0005
3	2	R(3)	2105.13	43.8	7469.43	0.0008 ± 0.0010
3	2	R(1)	2097.82	39.0	7443.24	0.0020 ± 0.0010
3	2	P(4)	2075.07	54.0	7454.47	0.0035 ± 0.0010
3	2	P(5)	2071.15	52.2	7469.42	0.0016 ± 0.0010
3	2	P(6)	2067.21	50.9	7488.12	0.0019 ± 0.0010
3	2	P(8)	2059.21	49.2	7536.73	0.0016 ± 0.0010
3	2	P(9)	2055.16	48.6	7566.64	0.0038 ± 0.0010
3	2	P(10)	2051.08	48.0	7600.28	0.0023 ± 0.0010
3	2	P(11)	2046.96	47.5	7637.65	0.0016 ± 0.0010
3	2	P(12)	2042.81	47.0	7678.76	0.0020 ± 0.0020
3	2	P(15)	2030.16	45.8	7824.46	0.0026 ± 0.0005
4	3	R(32)	2166.94	70.9	11566.89	0.0010 ± 0.0010
4	3	R(31)	2164.43	70.6	11445.50	0.0010 ± 0.0010
4	3	R(29)	2159.30	69.9	11213.62	0.0010 ± 0.0010
4	3	R(28)	2156.67	69.6	11103.12	0.0010 ± 0.0010
4	3	R(27)	2154.01	69.3	10996.28	0.0015 ± 0.0010
4	3	R(25)	2148.56	68.6	10793.52	0.0010 ± 0.0010
4	3	R(23)	2142.95	68.0	10605.36	0.0010 ± 0.0010
4	3	R(22)	2140.09	67.6	10516.78	0.0026 ± 0.0010
4	3	R(21)	2137.20	67.3	10431.87	0.0010 ± 0.0010
4	3	R(19)	2131.29	66.5	10273.04	0.0010 ± 0.0010
4	3	R(18)	2128.27	66.1	10199.13	0.0020 ± 0.0010
4	3	R(15)	2119.01	64.9	9999.49	0.0010 ± 0.0010
4	3	R(13)	2112.65	64.0	9884.82	0.0011 ± 0.0010
4	3	R(7)	2092.68	60.6	9629.41	0.0010 ± 0.0010
4	3	P(2)	2056.52	81.4	9499.76	0.0010 ± 0.0010
4	3	P(3)	2052.71	72.9	9507.17	0.0010 ± 0.0010

Table 2 continued

Table 2 (*continued*)

v'	v''	ID	$\tilde{\nu}$	A	E'	EqW
			cm^{-1}	s^{-1}	cm^{-1}	cm^{-1}
4	3	P(4)	2048.86	69.0	9518.28	0.0010 ± 0.0010
4	3	P(6)	2041.07	65.1	9551.62	0.0025 ± 0.0010
4	3	P(8)	2033.14	63.0	9599.77	0.0018 ± 0.0010
4	3	P(9)	2029.13	62.1	9629.41	0.0016 ± 0.0010
4	3	P(11)	2021.00	60.7	9699.76	0.0010 ± 0.0010
4	3	P(15)	2004.34	58.5	9884.82	0.0010 ± 0.0010
4	3	P(16)	2000.09	58.1	9940.31	0.0019 ± 0.0010
$^{13}\text{C}^{16}\text{O}$ lines						
1	0	R(30)	2193.13	18.2	4955.16	0.0010 ± 0.0010
1	0	R(28)	2187.89	18.0	4734.18	0.0010 ± 0.0010
1	0	R(23)	2174.17	17.6	4244.57	0.0019 ± 0.0010
1	0	R(22)	2171.31	17.5	4157.44	0.0014 ± 0.0010
1	0	R(21)	2168.42	17.4	4073.91	0.0010 ± 0.0010
1	0	R(16)	2153.44	16.9	3710.50	0.0013 ± 0.0010
1	0	R(13)	2144.03	16.6	3535.90	0.0027 ± 0.0005
1	0	R(10)	2134.31	16.2	3393.96	0.0046 ± 0.0005
1	0	R(9)	2131.00	16.0	3353.92	0.0032 ± 0.0005
1	0	R(7)	2124.29	15.7	3284.74	0.0017 ± 0.0010
1	0	R(5)	2117.43	15.2	3230.11	0.0023 ± 0.0010
1	0	R(4)	2113.95	14.9	3208.25	0.0026 ± 0.0010
1	0	R(3)	2110.44	14.5	3190.04	0.0017 ± 0.0010
1	0	R(2)	2106.90	13.9	3175.47	0.0011 ± 0.0010
1	0	P(1)	2092.39	31.8	3153.61	0.0013 ± 0.0010
1	0	P(3)	2084.94	18.8	3164.54	0.0025 ± 0.0010
1	0	P(7)	2069.66	16.5	3230.11	0.0042 ± 0.0010
1	0	P(9)	2061.82	16.1	3284.74	0.0038 ± 0.0020
1	0	P(10)	2057.86	15.9	3317.51	0.0026 ± 0.0010
1	0	P(12)	2049.83	15.6	3393.96	0.0028 ± 0.0010
1	0	P(13)	2045.78	15.4	3437.65	0.0035 ± 0.0005
1	0	P(15)	2037.57	15.2	3535.91	0.0038 ± 0.0010
1	0	P(16)	2033.42	15.0	3590.48	0.0028 ± 0.0010
1	0	P(17)	2029.24	14.9	3648.68	0.0025 ± 0.0005
1	0	P(19)	2020.78	14.7	3775.95	0.0033 ± 0.0010
1	0	P(21)	2012.21	14.5	3917.70	0.0018 ± 0.0010

Table 3. Line Profile Fit Parameters

Profile	a(0)	a(1)	a(2)	a(3)	a(4)	FWHM km s ⁻¹
¹² CO v=1-0	0.082±0.001	4.4±0.4	0	7.2±0.1	1.0024±0.0001	19.51±0.27
¹² CO v=2-1	0.021±0.001	30.1±9.1	0	5.8±0.5	1.0046±0.0001	22.64±0.66
¹² CO v=3-2	0.013±0.003	32.1±17.5	0	6±4	1.0002±0.0001	22.17±1.07
¹² CO v=4-3	0.004±0.003	200±200	0	5±7	1.005±0.001	...
¹³ CO v=1-0	0.016±0.001	8±3	0	6.4±0.9	1.005±0.0001	20.15±0.91

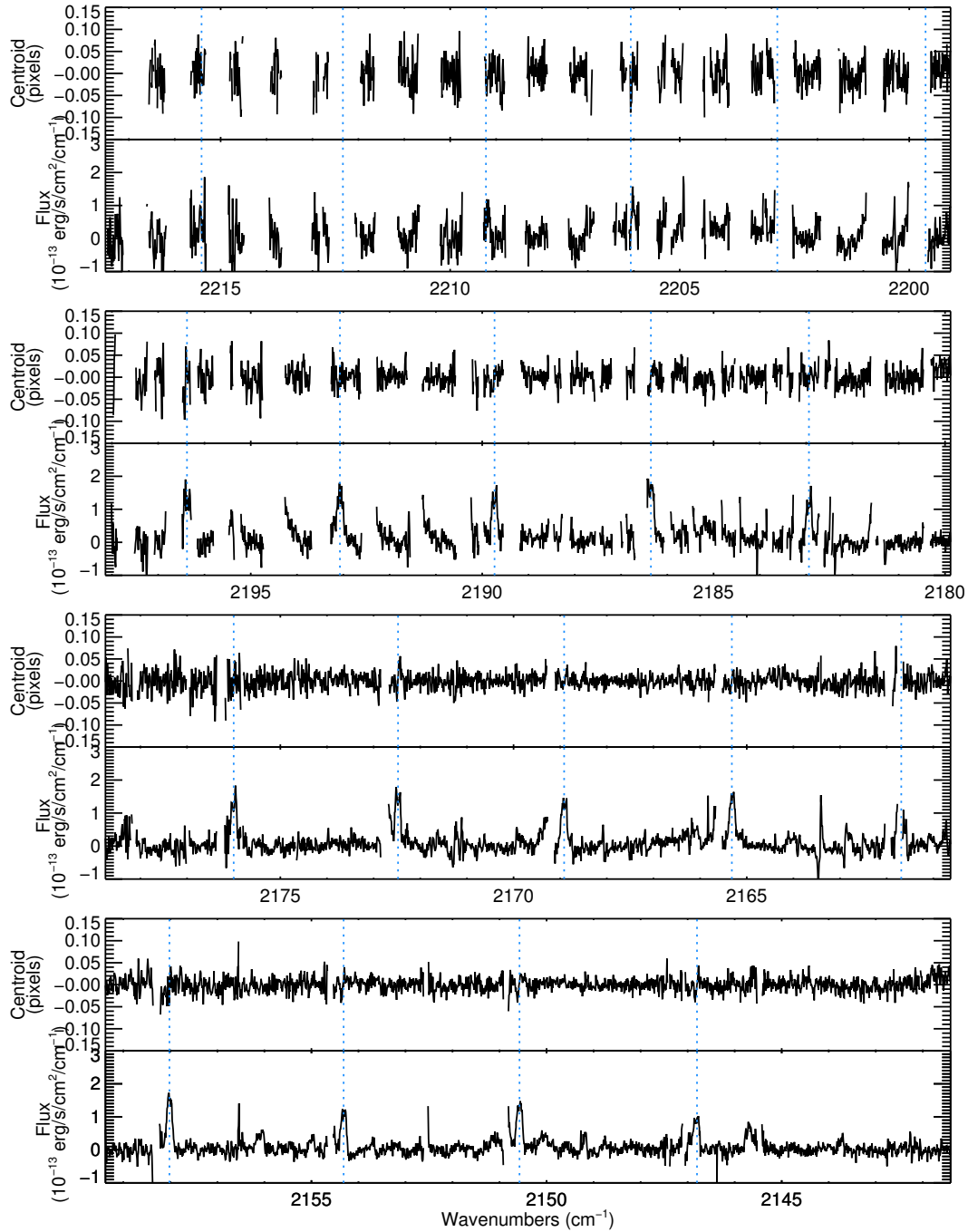


Figure 1. M -band spectrum of HD 179218. The spectrum of HD 179218 is plotted in the lower panel and the relative centroid of the PSF is plotted in the upper panel. Gaps in the spectra are regions where the atmospheric transmittance is less than 50%. The positions of the $v=1-0$ CO lines are marked with dotted vertical lines (blue).

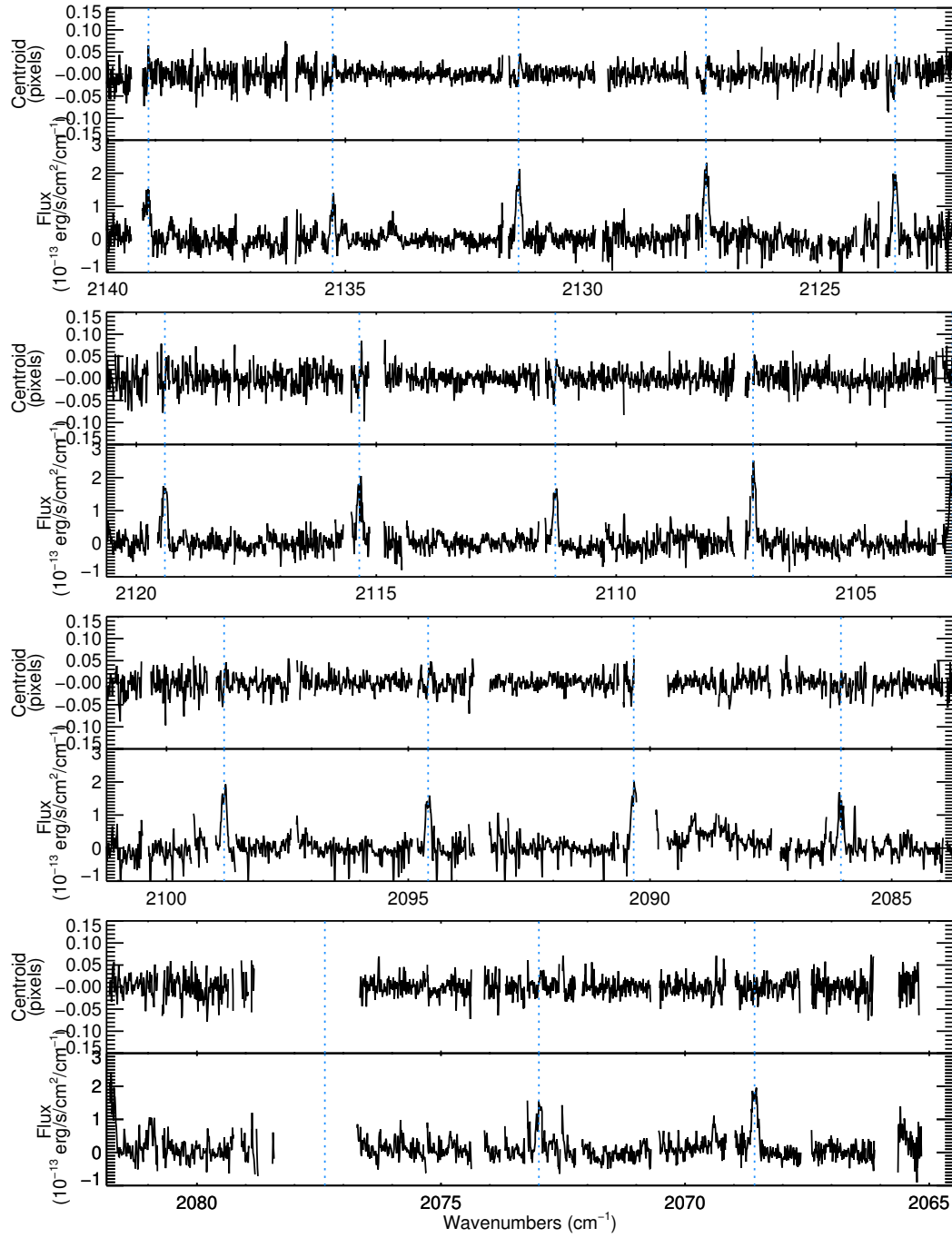


Figure 1. cont

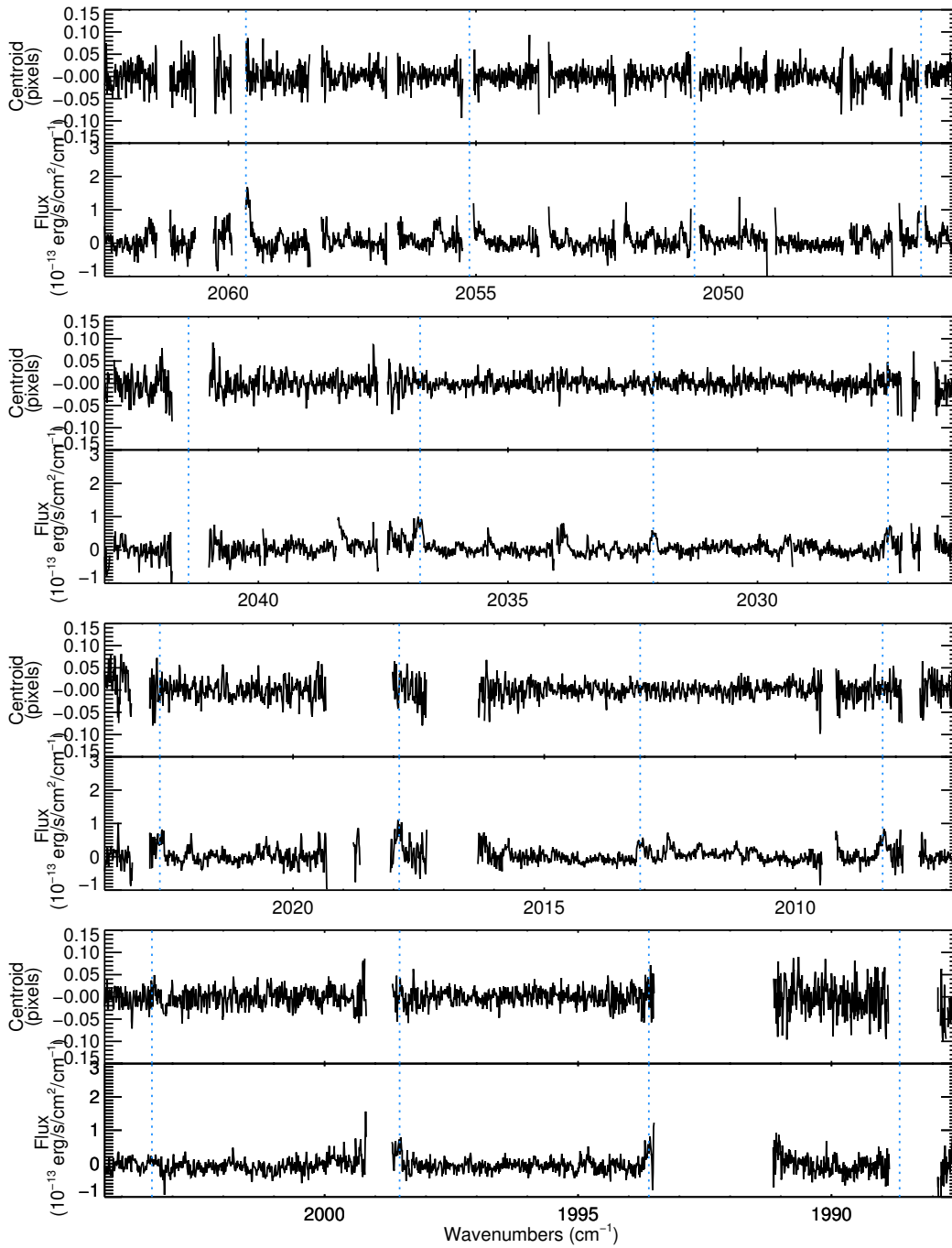


Figure 1. cont

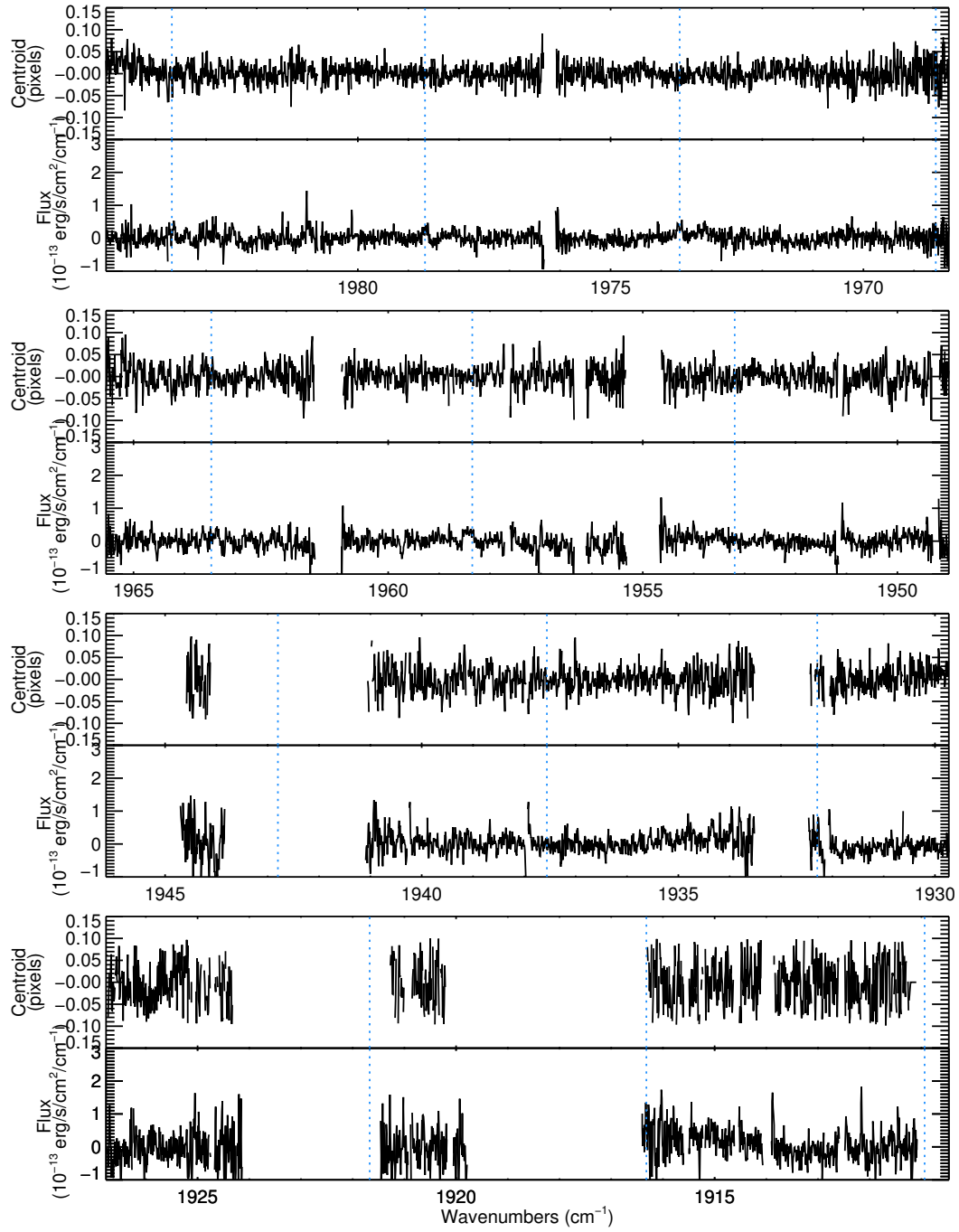


Figure 1. cont

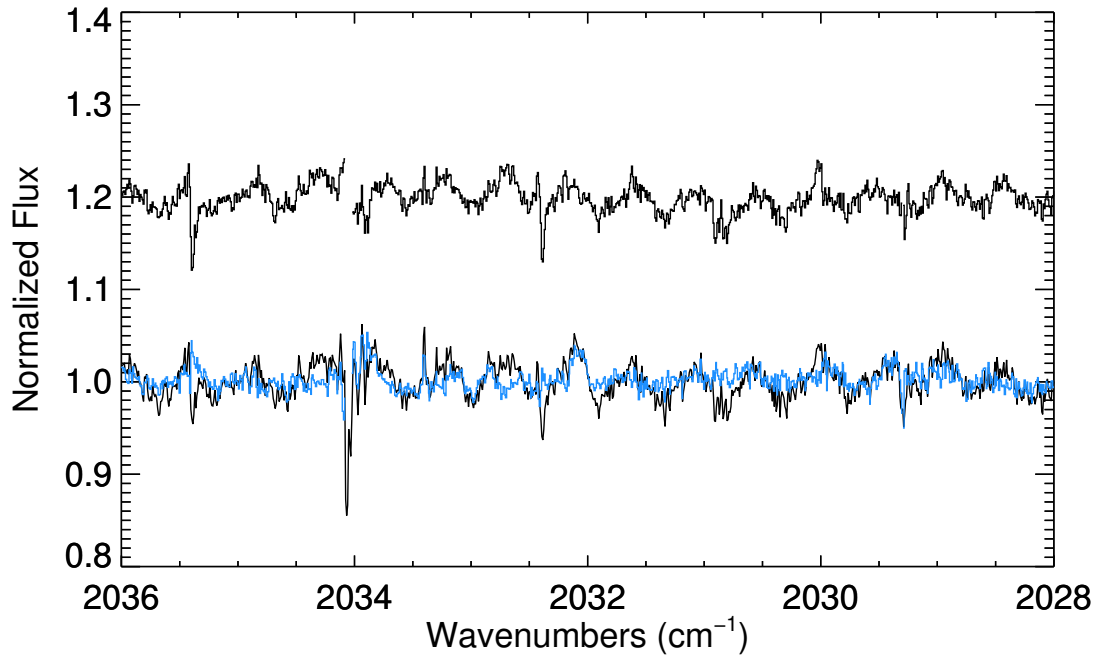


Figure 2. Sample spectrum of HD 179218 illustrating fringing. This region was selected due to the minimal telluric features. Rather than dividing by the telluric standard, the atmospheric lines were corrected with the SSP model (black line). The fringe is $\sim 5\%$ of the continuum in this region which is representative of the spectrum. Telluric correction with a standard star taken without having moved the grating between observations corrects the fringe (blue line). The difference between the two versions is plotted above.

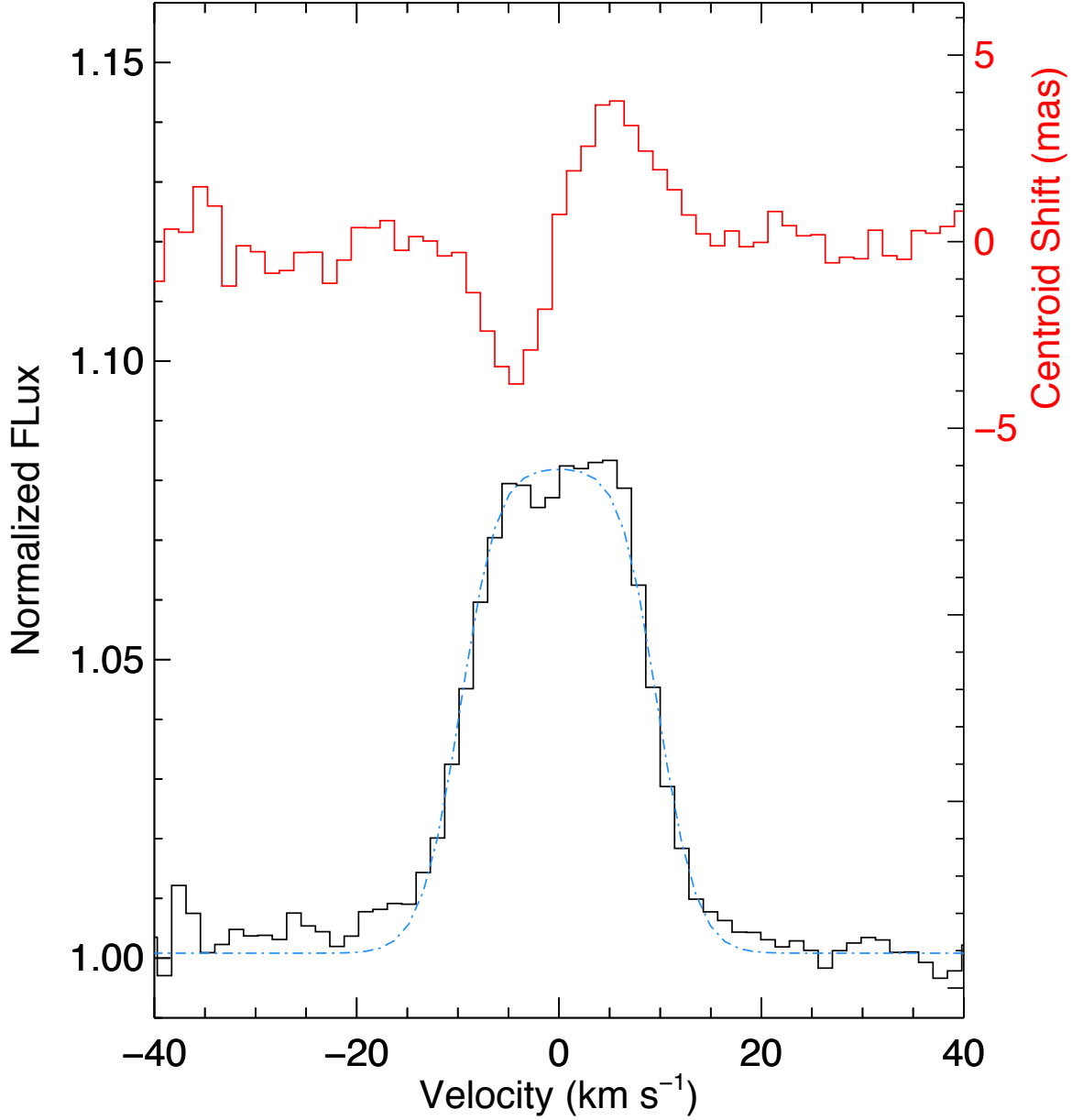


Figure 3. Profile of $v=1-0$ CO lines and spectroastrometric signal. The average profile of the $v=1-0$ spectral lines (black), a functional fit to the line profile (blue), and their spectro-astrometric signals (red) are plotted versus velocity. The FWHM of the emission line is 19.51 ± 0.27 km s $^{-1}$. The blip near -40 km s $^{-1}$ is the location of the low-J CO telluric lines. Since this region is excluded from the average for the low-J lines, the SNR of this part of the average spectrum is lower. The SNR of the continuum is 520 and the pixel to pixel standard deviation of the spectro-astrometric signal is 0.44 mas.

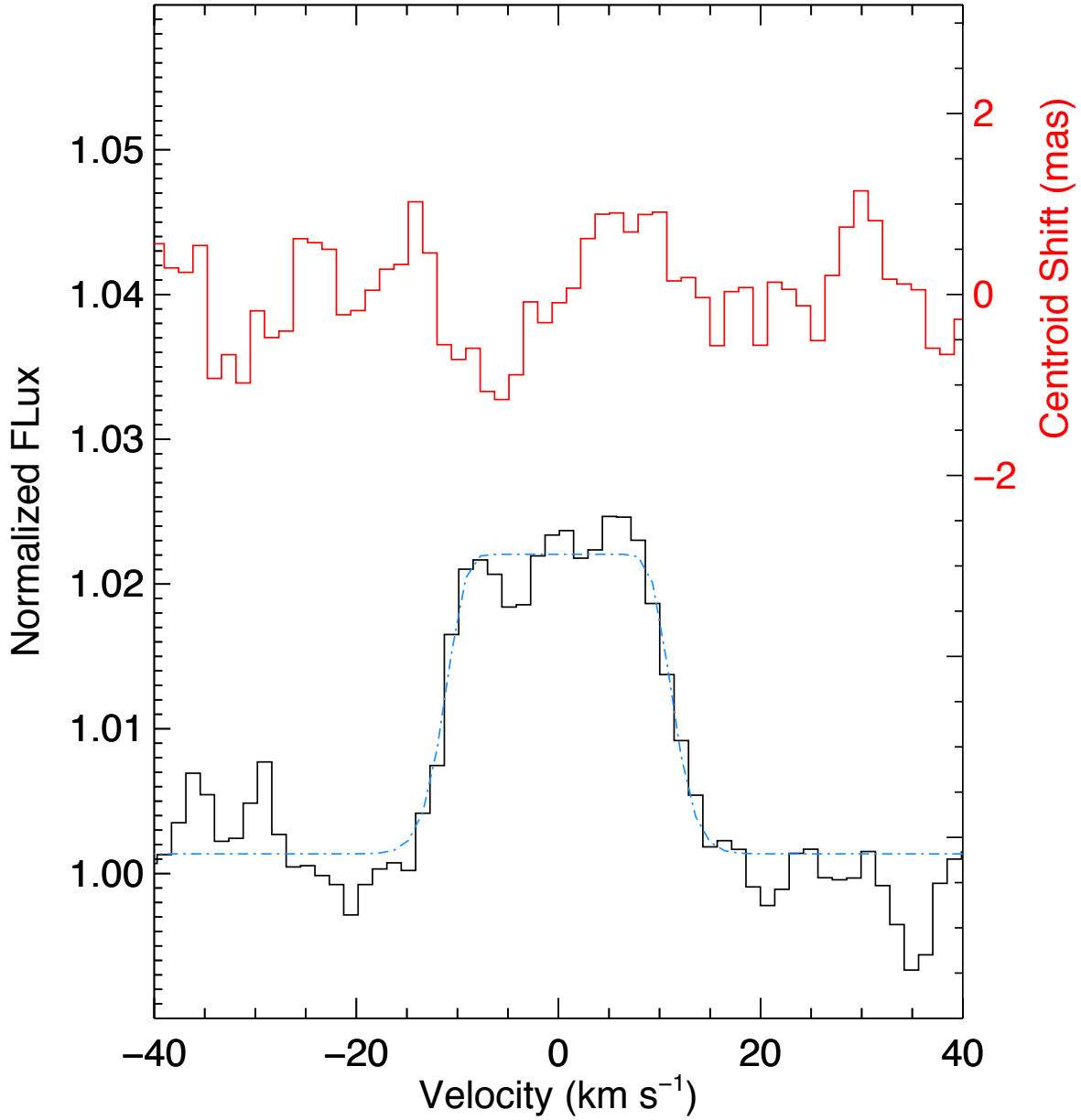


Figure 4. Profile of $v=2-1$ CO lines and spectro-astrometric signal. The average profile of the $v=2-1$ spectral lines (black), a functional fit to the line profile (blue), and their spectro-astrometric signals (red) are plotted versus velocity. The FWHM of the emission line is $22.64 \pm 0.66 \text{ km s}^{-1}$.

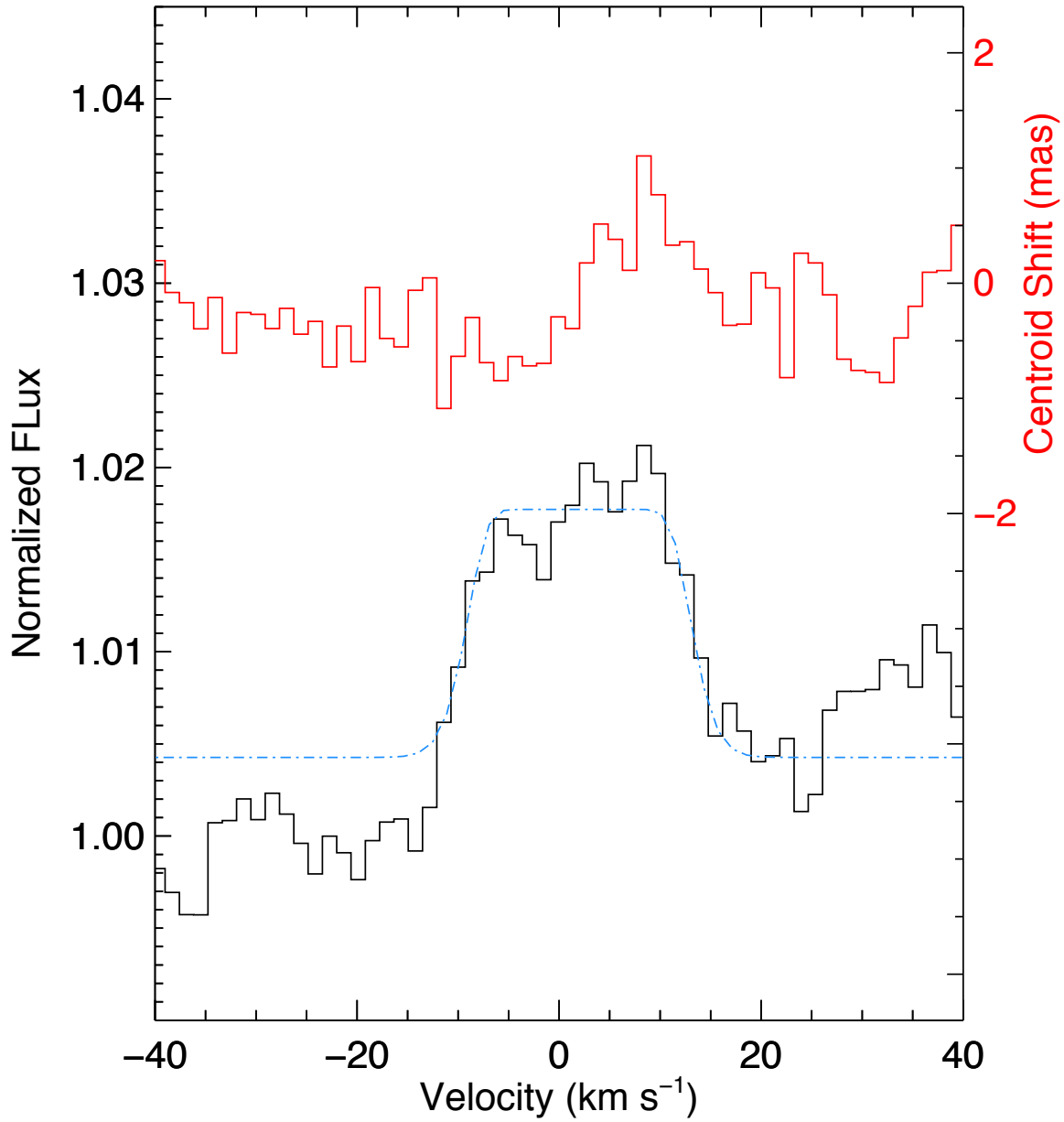


Figure 5. Profile of $v=3-2$ CO lines and spectro-astrometric signal. The average profile of the $v=3-2$ spectral lines (black), a functional fit to the line profile (blue), and their spectro-astrometric signals (red) are plotted versus velocity. The FWHM of the emission line is 22.17 ± 1.07 km s⁻¹.

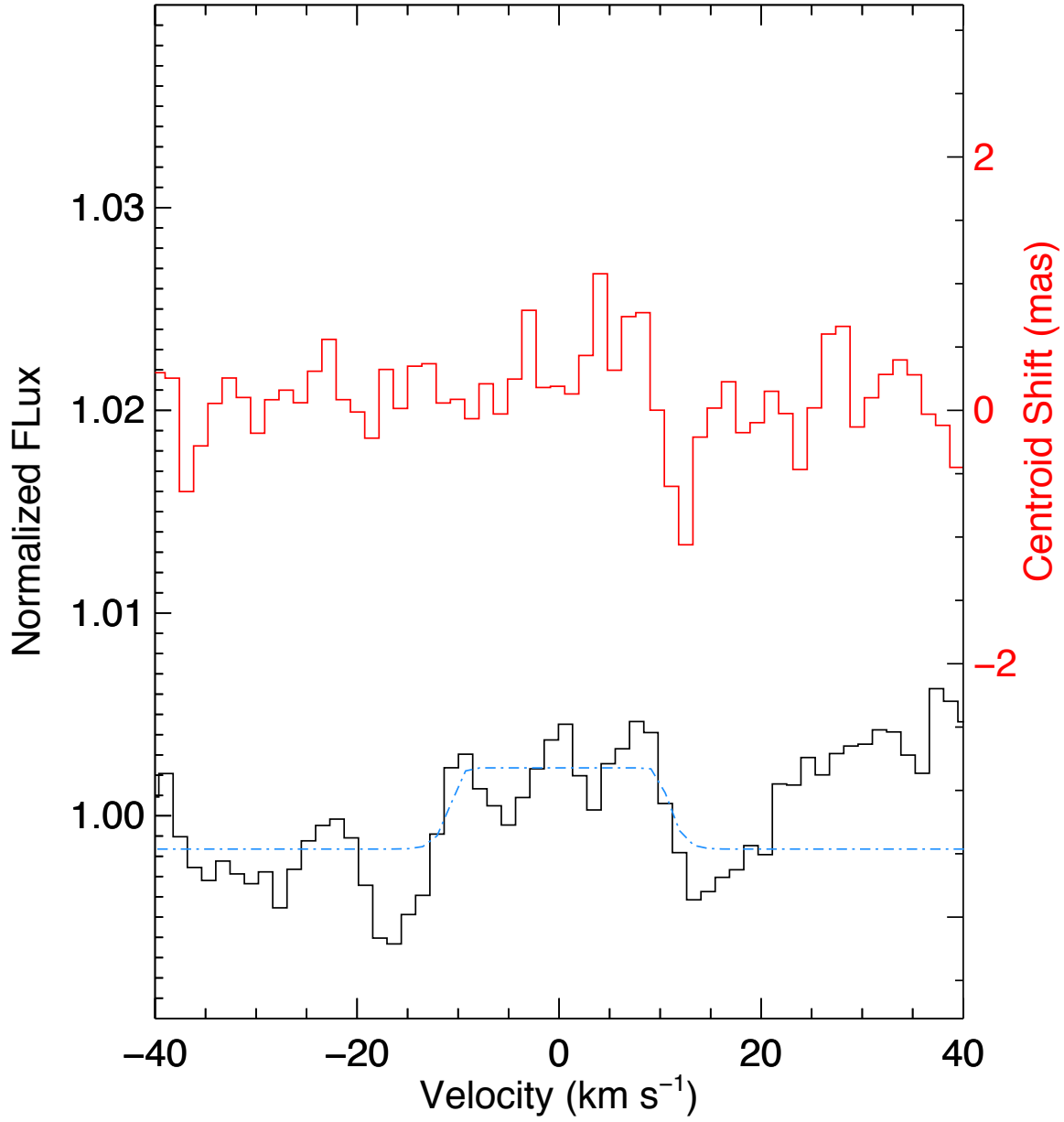


Figure 6. Profile of $v=4-3$ CO lines and spectro-astrometric signal. The average profile of the $v=4-3$ spectral lines (black), a functional fit to the line profile (blue), and their spectro-astrometric signals (red) are plotted versus velocity. The $v=4-3$ lines are not detected.

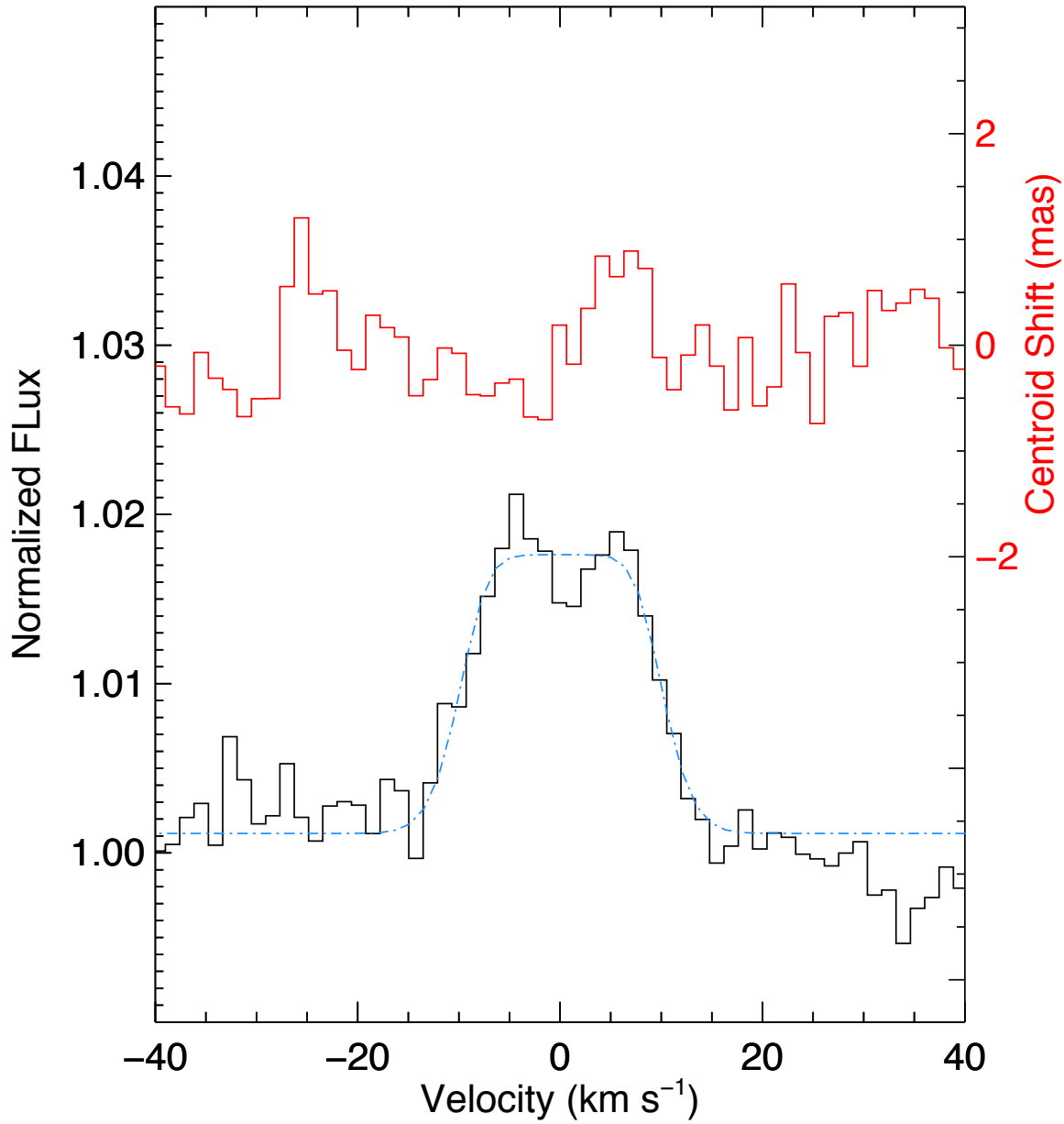


Figure 7. Profile of ^{13}CO lines and spectro-astrometric signal. The average profile of the $v=1-0$ spectral lines (black), a functional fit to the line profile (blue), and their spectro-astrometric signals (red) are plotted versus velocity. The FWHM of the emission line is $20.15 \pm 0.91 \text{ km s}^{-1}$.

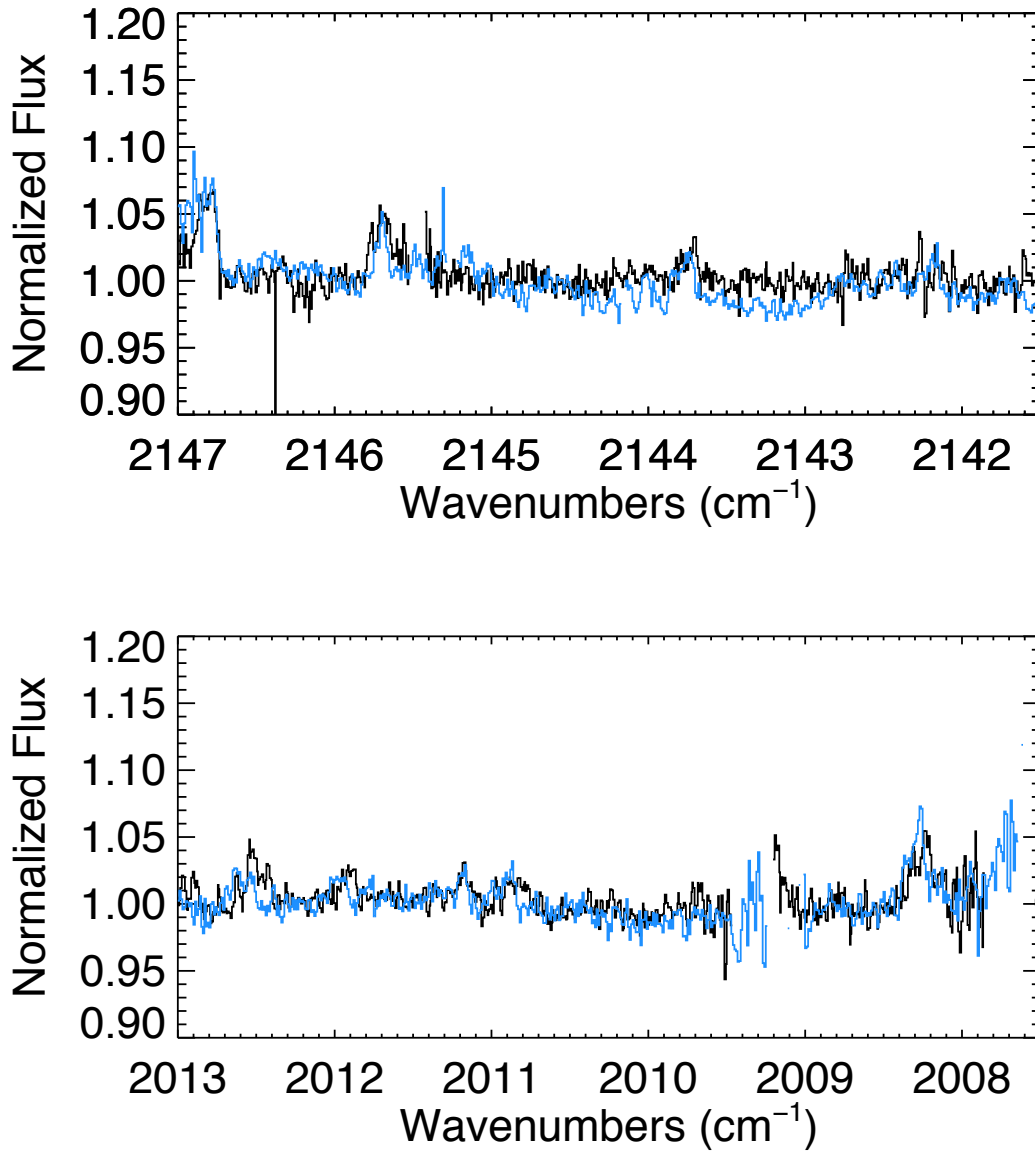


Figure 8. Comparison of spectrum acquired with CRiRES. The spectrum acquired with iSHELL (black) is plotted with the spectrum acquired with CRiRES (blue). These regions were selected to minimize systematic features from miscanceled telluric lines. The per pixel SNRs of the continua near 2145cm^{-1} and 2011.5cm^{-1} are 120-130 in the iSHELL spectrum and the CRiRES spectrum. The iSHELL spectrum was the result of 30 minutes of integration. The integration times of the CRiRES spectra were 20 minutes and 16 minutes respectively.

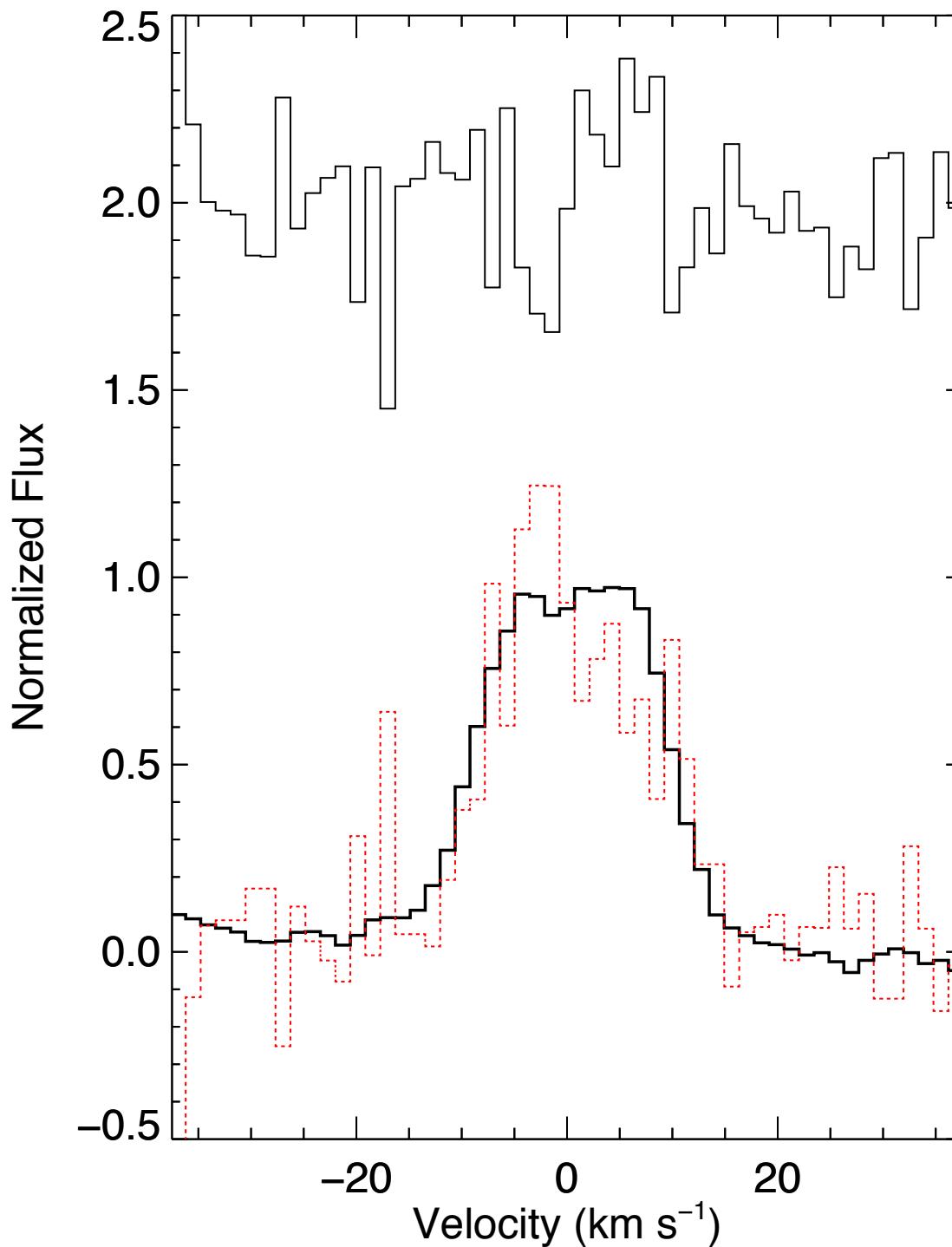


Figure 9. Comparison of the $v=1-0$ CO line profile constructed from data acquired with iSHELL and CRILES. The average profile of the $v=1-0$ lines observed with iSHELL (black) is plotted over the average profile of the $v=1-0$ lines observed with CRILES (red). The line profiles have been scaled to a common equivalent width. The difference between the profiles is plotted above. The signal to noise ratio of the profile improved by a factor of 10 due to the large increase in the number of lines included in the average. The iSHELL spectrum was the result of 30 minutes of integration. The integration time of the CRILES spectrum was 46 minutes. While there is some indication of an asymmetry in the profile constructed from lines observed with CRILES, the signal to noise ratio is too low to conclude anything definitive.

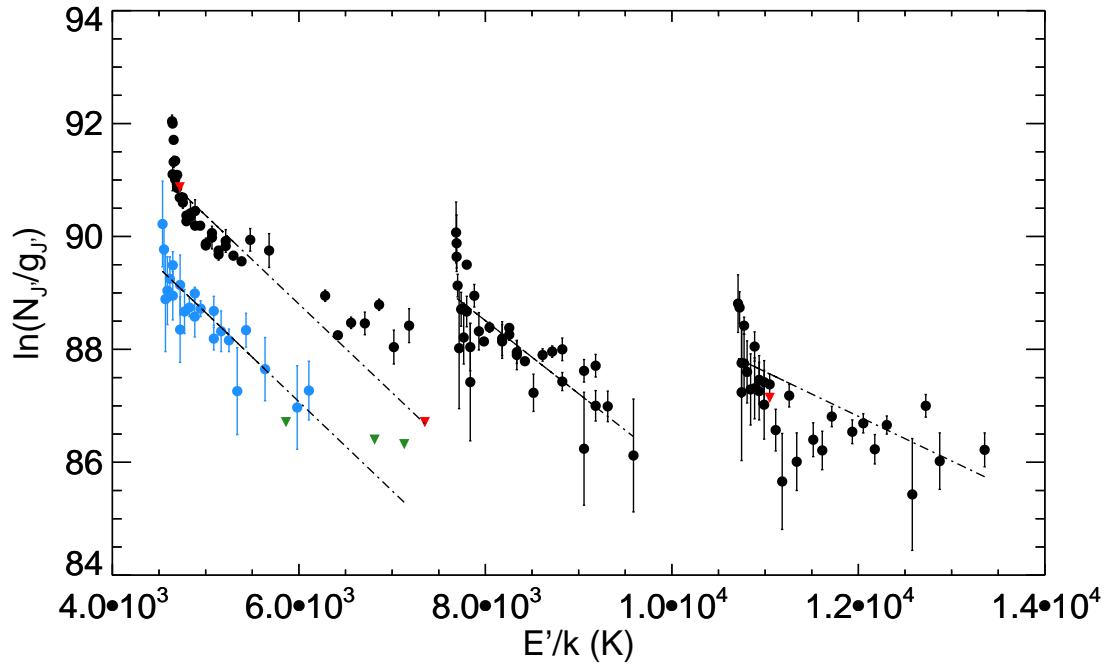


Figure 10. Excitation diagram of CO emission from HD 179218. E'/k is plotted versus $\ln(N'_J/g'_J)$. The detected $^{12}\text{C}^{16}\text{O}$ lines are plotted with black points and the upper limits are plotted with red downward pointing triangles. The detected $^{13}\text{C}^{16}\text{O}$ lines are plotted with blue points and the upper limits are plotted with green downward pointing triangles. There were no individual lines from the $v=4-3$ vibrational band detected. The rotational temperatures of the $^{12}\text{C}^{16}\text{O}$ $v=1-0$, $v=2-1$, $v=3-2$, and $^{13}\text{C}^{16}\text{O}$ $v=1-0$ lines are 640 ± 10 K, 770 ± 30 K, 1270 ± 120 K, and 630 ± 90 K respectively. The vibrational temperature is 1850 ± 90 K.